Dynamic bonding influenced by the proximity of adatoms to one atom high step edges

W. Dednam [1,2] S. Tewari [3] E. B. Lombardi [1] J. J. Palacios,[4] J. M. van Ruitenbeek [3] and C. Sabater [2,*]

[1]*Physics Department, College of Science, Engineering and Technology, University of South Africa, Private Bag X6, Florida Park, Johannesburg 1710, South Africa*
[2]*Departamento de Física Aplicada and Unidad asociada CSIC, Universidad de Alicante, Campus de San Vicente del Raspeig, E-03690 Alicante, Spain*
[3]*Huygens-Kamerlingh Onnes Laboratorium, Leiden University, Niels Bohrweg 2, 2333 CA Leiden, The Netherlands*
[4]*Departamento de Física de la Materia Condensada, Condensed Matter Physics Center (IFIMAC) and Instituto Nicolás Cabrera, Universidad Autónoma de Madrid, Madrid E-28049, Spain*

Low-temperature scanning tunneling microscopy is used here to study the dynamic bonding of gold atoms on surfaces under low coordination conditions. In the experiments, using an atomically sharp gold tip, a gold adatom is deposited onto a gold surface with atomic precision either on the first hollow site near a step edge or far away from it. Classical molecular dynamics simulations at 4.2 K and density-functional theory calculations serve to elucidate the difference in the bonding behavior between these two different placements, while also providing information on the crystalline classification of the STM tips based on their experimental performance.

I. INTRODUCTION

The scanning tunneling microscope (STM) [1,2] is the most common scientific instrument used to obtain the topography of nanometer-sized areas with subatomic precision [3,4]. When this instrument is combined with high vacuum and low-temperature (LT) conditions, its capabilities increase, also allowing for atomic manipulation [5–9]. Essentially, there are two modes of operation for the LT-STM. First, the noncontact mode, that uses the tunneling current to scan and manipulate atoms on the surface. Second, the contact mode where bonding between apex tip atom and adatoms on the surface is allowed. This second mode is based on a gentle atomic touch and it is used to manipulate, move, or deposit adatoms onto the surface. In both modes the integrity of the tip and the surface should be preserved [10].

For atomic manipulation, the atoms on the apex of a STM tip need to establish a bond with the atoms on the surface through the sharing of electrons. The process that occurs in going from the tunneling regime to the atomic contact is called dynamic bonding, and it is usually studied through the changes in the conductance during this process. Electron transport at these atomic scales is usually described by Landauer formalism [11] where the quantum of conductance, $G_0 = 2e^2/h$ (e is the charge of the electron and h is Planck's constant) acts as a reference quantity. Depending on the nature of the electrodes, the conductance can exhibit a discontinuity from the last point of tunneling to the contact point, a phenomenon which is named "jump-to-contact" (JC). Other than the technique of landing the STM tip over target adatoms or molecules [12,13], this phenomenon has also been extensively reported in experiments using the mechanically controlled break junction (MCBJ) technique [14–16] and the STM in the break-junction approach [17–25].

In this work we use the LT-STM technique to manipulate adatoms at will so that we can study the JC phenomenon in controlled environments. In particular, we have considered two scenarios where the STM tip is used to probe an adatom (1) located in a hollow site on a flat Au(111) surface and (2) placed close to a one-atom-high step edge. These two scenarios were selected because they provide the most detailed control over the atomic positions, while potentially leading to the largest differences in bonding environment. We complement the LT-STM-BJ experimental results with classical molecular dynamics (CMD) simulations and density-functional theory (DFT) calculations for quantum transport. Although related theoretical results have been previously reported [26], the triple combination of these techniques is used here for the first time to get a full picture of electronic and mechanical properties of adatoms close and far away from the edge-steps. Further, our combination of techniques allows to learn about the integrity of the tip in the experiments, offering a nondestructive new approach to get information about the tips' geometry which is *a priori* impossible to obtain just from the experiments. Understanding the tip deformation allows new insights in the field of atomic manipulation, and molecular electronics. However, the detailed study of the deformation of the surface during the dynamic bonding process opens the door to unmasking mechanisms and understanding effects in the emerging field of straintronics.

II. EXPERIMENTAL APPROACH

An ultra high-vacuum low-temperature STM in the break junction configuration is used in this work to control the
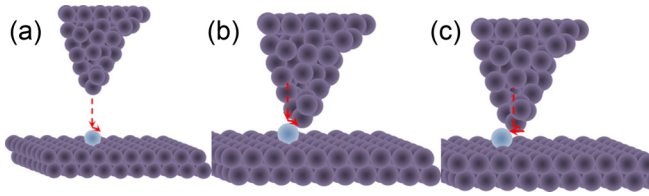
---

*carlos.sabater@ua.es

FIG. 1. Point-contact push (PCP) technique: (a) The STM tip is positioned directly above the adatom before a point contact is made and then brought vertically downwards. (b) Once contact has been made the STM tip is moved in a circular trajectory while remaining in contact with the adatom until the tip is behind it. (c) When the tip is positioned behind the adatom it pushes the latter to the next hollow site.
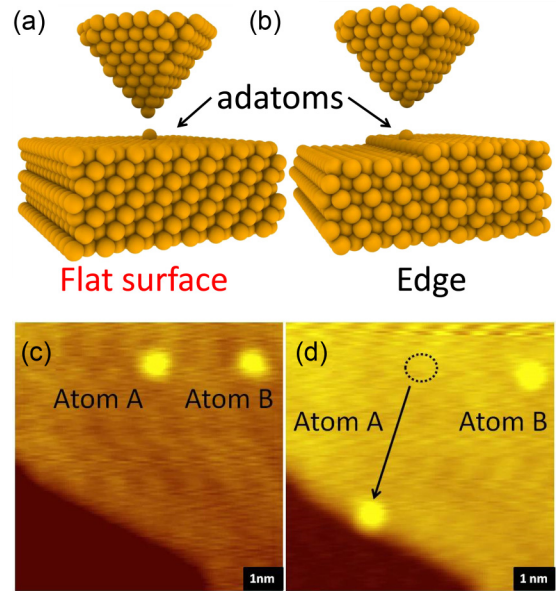

FIG. 2. Illustration of a STM tip and an adatom on a surface (a), all composed of gold atoms, and (b), the same STM tip and adatom close to a step edge that is one-atom high. (c) STM image of the surface with 2 adatoms labeled A and B. (d) STM image after the new position of the A atom which was moved in the first hollow directly above the step edge.

motion and manipulate the position of a single adatom on a surface and measure the electronic transport. To improve the control of the STM tip and the adatom, a real-time molecular dynamics simulator and a 3D motion control system have been incorporated in this experimental setup [27–29]. To emulate the experiment and permit synchronization with the 3D motion system, there are only a few atoms interacting via low computational cost potentials in the real-time molecular dynamics simulator.

The surface sample consists of monocrystalline gold cut along the (111) crystallographic direction. It is prepared together with the Au tip by repeated argon sputtering and thermal annealing cycles, to obtain an atomically flat Au(111) facet showing herringbone surface reconstruction. We further prepare the surface at low temperature through the creation of a localized stress pattern [30–33] using gentle indentation of the STM tip at a spot on the surface removed from the area of investigation. This controlled crash of the tip onto the surface produces new crystalline (111) facets, and straight step edges in the three crystallographic directions of Au(111). Furthermore, to make an atomically sharpened gold tip we follow the procedure detailed in Refs. [10,34,35]. Additionally, gold atoms are deposited [8,28,35,36] on the Au(111) surface at the target sites of investigation [Fig. 2(c)], and the procedure by which they are manipulated is described briefly below. All the STM experiments were carried out at a temperature of 4K, under ultrahigh vacuum. The gold tip was obtained by indenting a freshly etched platinum tip into the gold surface and repeated mechanical annealing [10,35].

To move adatoms near these one-atom-high step edges, we need to know the configuration of the substrate atoms close to the edge. The atomic configuration of metallic surfaces like Au(111) is not readily available in STM images due to the delocalized nature of the valence electrons in metals [37]. However, following the protocol designed by Tewari *et al.* [28,35] and appealing to geometric arguments, it is possible determine the orientation of the Au(111) substrate. Once the substrate atomic configuration is known, an adatom can be moved to the step edge using the point-contact pushing (PCP) technique, which involves maintaining contact between the adatom and tip, while the tip is lowered from the point of first contact by approximately a quarter of the atomic height, with the help of the 3D motion control system.

As shown in Fig. 1, the tip starts over the adatom (a), and is lowered into the pushing position (b), and the adatom is

pushed from one hollow site to another (c), while obtaining visual feedback from the real-time simulation, which helps to precisely place the adatoms at a target site near the step edge.

The dynamic bonding can be studied via STM-BJ experiments [17–19], for adatom positions in the middle of the surface, or just in the first hollow site after the step edge. In the Introduction we defined dynamical bonding as the process that occurs in going from the tunneling to the atomic contact regimes. This dynamical bonding is observed in the form of a "jump-to-contact" (JC) [22]. The JC is manifested, notably for noble metals, when atomically sharp electrodes approach each other, and the measured conductance jumps from the tunneling regime ($\lesssim 10^{-1}G_0$) to atomic contact ($\approx G_0$).

In the STM-BJ experiments carried out in this work, after completing the PCP maneuver, placing the adatoms at their respective sites, the tip is then located directly above the adatom and slowly lowered toward it. During this process the current that flows as the tip approaches the surface is measured. In the experiments this current was amplified and converted to voltage by a Femto I/V (model DLPCA-200) using the amplification 10^6 V/A. Knowing that the bias voltage applied over the tip and surface is 100 mV, the conductance can be expressed as $G = 1/R = V/I$, and converted to quantum of conductance units, with $G_0 = \frac{1}{12906}\Omega^{-1}$. The curve of conductance versus the voltage applied to the piezo system is called a contact formation or contact breaking trace. In this study of the JC we focus on contact formation traces.

III. EXPERIMENTAL RESULTS

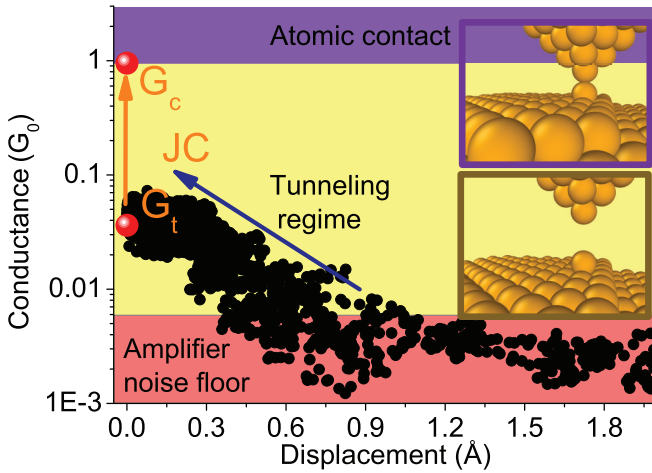To reproduce the scenarios illustrated in Figs. 2(a) and 2(b), we have evaporated gold adatoms onto a surface of

FIG. 3. Experimental trace of conductance for adatom on a edge in semilogarithmic scale. The horizontal axis starts from an arbitrary zero-point. Red area shows the amplifier noise floor, yellow area highlight the tunneling regime and the purple area reflects where the atomic contact occurs. The points G_t and G_c are highlighted in red from the remaining points of the trace. Atomic contact and tunneling regimes are illustrated in the insets, respectively. The coloring of the inset frames corresponds to the previously described coloring regimes.

gold oriented in the (111) crystallographic direction with step edges as shown in Fig. 2(c).

The scan in Fig. 2(c) shows that there are two adatoms (atoms A and B) close to each other on an Au(111) facet. Through use of the PCP technique, we moved atom A from its original position to the new position at the first hollow site directly above the step edge, as shown in Fig. 2(d), where the black circle indicates the original position of atom A, and an arrow its trajectory from the old to the new position close to the edge. To refer to the states of adatoms A and B in Fig. 2(d), we have used the nomenclature of "edge" for A and adatom on the "flat surface" for B.

Once the atoms are positioned at the edge or in the flat surface region far from the edge, we proceed to study the dynamic bonding of each of these adatoms to the tip by means of the JC phenomenon. We recorded traces of contact formation starting from the tunneling regime until contact was established between a single atom of the tip and the respective adatom (which occurs at $\approx 1 G_0$).

Figure 3 shows a trace of conductance during the approach process of the tip toward the adatom directly below it, which is located close to the edge [see Fig. 2(b) and atom A of Fig. 2(d)]. In Fig. 3 the pale red area contains the amplifier noise floor values for the trace of formation. The blue arrow indicates the direction in which trace of conductance should be read. The yellow area corresponds to the tunneling regime, prior to contact. The values of the illustrative jump-to-contact (JC) which spans from $G_t = 0.05 G_0$ to contact at $G_c = 0.95 G_0$ are highlighted from the rest of the trace by two red solid circles. The orange arrow shows the abrupt jump in the conductance. The purple area represents the region of the atomic contact. Finally, the insets of Fig. 3 illustrate the

TABLE I. Jump-to-contact values for adatoms on the **Edge** and **Flat surface**. The results of the jump-to-contact are expressed in pair of values (G_t, G_c) in units of G_0.

Trace Formation	Edge (G_t, G_c)	Flat surface (G_t, G_c)
01	(0.17, 0.95)	(0.04, 0.93)
02	(0.07, 0.94)	(0.05, 0.93)
03	(0.05, 0.96)	(0.04, 0.95)
04	(0.05, 0.96)	(0.01, 0.91)
05	(0.06, 0.96)	(0.02, 0.94)
06	(0.04, 0.95)	(0.08, 0.94)
07	(0.03, 0.96)	(0.03, 0.94)
08	(0.08, 0.96)	(0.03, 0.92)

the contact and tunneling regimes, marked by purple and dark yellow borders, respectively.

We recorded eight traces of conductance in each scenario. From each trace we have extracted the pairs of points that represent the JC, which are labeled as G_t and G_c. The latter is the first conductance value that is measured just after JC has occurred. Consequently, G_t is taken as the value that is measured immediately before G_c. Table I shows measured values of (G_t, G_c) in each scenario. The precise preparation of the environment of the adatom sites and the reproducible tip preparation procedure result in small variations of the values between the eight attempts. Nevertheless, some variation remains, as may be expected for a process that is associated with a dynamic instability. Note that the noise level in the conductance regime shown in Fig. 3 agrees with the variation of G_t in Table I.

To summarize the results shown in Table I we have calculated the mean values and the standard deviations of G_t and G_c (see Table II). We find that the last conductance before the jump into contact (G_t) to within our experimental accuracy does not depend on the positioning near the edge. However, the first contact (G_c) values differ between the edge and flat surface scenarios.

IV. THEORETICAL MODEL

The STM technique allows the creation of different geometric scenarios and permits a study of the electronic transport, to assess whether or not bonding has occurred. However, classical molecular dynamics (CMD) gives us the ability to simulate the experiment atomistically, allowing us to estimate atomic structures and interatomic distances during adhesion, explaining the mechanisms underpinning the process of adhesion. The combination of DFT and

TABLE II. Mean values and standard deviations of G_t and G_c of the data shown in Table I.

Scenario	G_t (G_0)	G_c (G_0)
Edge	0.07 ± 0.04	0.96 ± 0.01
Flat surface	0.04 ± 0.02	0.93 ± 0.01

nonequilibrium Green's function techniques (NEGF) allows us to determine conductance values for the structures obtained from CMD, permitting comparison with experimental conductance values for the respective contact scenarios, prior to the tips making contact.

A. Classical molecular dynamics simulations

To imitate the experiments, we have simulated the two different scenarios represented by Figs. 2(a) and 2(b), respectively. Thus, Fig. 2(a) shows an atomically sharp gold tip directly above an adatom on top of an otherwise smooth surface, and Fig. 2(b) shows the same tip above an adatom close to a step edge. Each also represents the initial structures used in the respective simulations, prior to the tips making contact.

Classical molecular dynamics (CMD) is based on solving the second Newton's law to obtain the trajectory of every atom during a simulation [38,39]. In this way, we can trace the evolution of a collection of atoms in real-time, and at a very fine time resolution ($\sim$1.0 femtosecond in our case). The interaction between the atoms in the simulation is usually derived semiempirically, with the many-body potential being fitted to a number of physical properties of the material, obtained experimentally and/or by means of first-principles quantum mechanical calculations. Here, we use the semiempirical many-body embedded atom method (EAM) [40] with the interatomic potential described by Zhou *et al.* [41,42]. This potential reproduces the elastic and mechanical properties of atomic-sized gold contacts surprisingly well [25,26].

In this work, we use the LAMMPS [43,44] CMD code to model a gold tip interacting with a gold surface oriented along the [111] crystallographic direction (see Fig. 2), to generate these tip-adatom-surface structures. The adatom on a flat surface, Fig. 2(a), or at an edge, Fig. 2(b), contain a total of 1830 and 1746 atoms, respectively. To move the tip toward the respective adatoms, we freeze the internal positions of the atoms in the topmost layers of the tip, which are then moved downwards. The lowest layers of the substrate gold surface are also frozen internally and moved upwards. The combined speed of approach between tip and surface is $\sim$1.0 m/s. The remaining atoms of the tip-surface system respond dynamically to the motion of these frozen layers and, in this way, tip and surface (with adatom on top) are pushed together to make contact. The surfaces are periodic in the x- and y-directions. The speed with which the approach occurs may be several orders of magnitude higher than in an actual experiment, but it is still low enough for the atoms to reach equilibrium between thermostating to the target temperature, which is effected every 1000 time steps by means of the Nose-Hoover thermostat [45,46]. This particular thermostat was chosen since it reproduces the canonical ensemble even in the presence of an external force such as that applied to move our tip and surface [39]. For integration of the trajectory of the system, the Velocity-Verlet algorithm was used [39,47], with an integration time step of 1 fs.

To determine when first-contact occurs, we have established the next criteria. First of all, in our simulations we record the distance between the apex atom of the tip and the adatom. We assumed that the first contact occurs when these two atoms are within a distance of each other that is halfway between first and second nearest neighbors in a perfect FCC lattice. In the case of gold this corresponds to 3.48 Å. Once contact is detected the first point of contact and the last point of the approach can be identified. To compare this with the corresponding experiment, we need to calculate electronic transport for the scenarios of precontact and first point of contact.

B. Electronic transport calculations

In this work, we have computed the electronic transport using DFT+NEGF. We use the nonequilibrium Green's function (NEGF) approach to quantum scattering, in particular, the Keldysh formulation thereof [48–50]. This method has been implemented in the Atomistic Nano Transport (ANT.G) code [51], which interfaces with the quantum chemistry DFT code GAUSSIAN [52]. ANT.G divides the nanocontact into a semi-infinite lead-device-semi-infinite lead configuration. GAUSSIAN then calculates, within the local spin density approximation of the exchange-correlation function of DFT, the electronic structure of the device region, including a portion of the semi-infinite leads on both sides of the device. The extended leads (constructed as Bethe lattices) are, in turn, described electronically by Slater-Koster tight-binding parameters [49]. The calculations would become costly if all the atoms in a given CMD snapshot were included. Therefore, before performing conductance calculations, we trim down our CMD snapshots to fewer than 400 atoms. The trimmed-down structures are centered on the region of first contact. Furthermore, to obtain accurate results, we assign an 11-electron *spd*-orbital basis set to around 100 atoms in the constriction [26,53]. The remaining atoms are assigned a one-electron 6*s*-orbital basis set.

V. THEORETICAL RESULTS

To imitate the experimental approach of continuous cycles of repeated contact formation and breaking, our CMD simulations are similarly performed. A total of 10 continuous cycles of rupture and formation are simulated for each scenario of the adatom (near the edge or on a flat surface, respectively). The conductance for the tunneling G_t and contact G_c regimes are then determined according to the approach described in the previous section, for each of the cycles, for each of the two adatom scenarios.

Thus, mirroring the experimental approach, we can represent the vertical distance between the adatom and tip apex atom vs. simulation time step, as shown in Fig. 4. Both the flat surface and edge scenarios are shown, with light red dots corresponding to the adatom in the flat surface region, and black dots for adatoms located in the first hollow site on top of the atomic step. For the sake of comparison with the experiment, we refer to this type of plot as a distance trace. In Fig. 4 the traces of distance correspond to cycle number 5 in both scenarios. The dashed rectangle in the upper panel is magnified in the bottom panel to show more clearly how the simulated jump-to-contact occurs. The jump seems to occur less abruptly when the adatom is near an edge, while, when
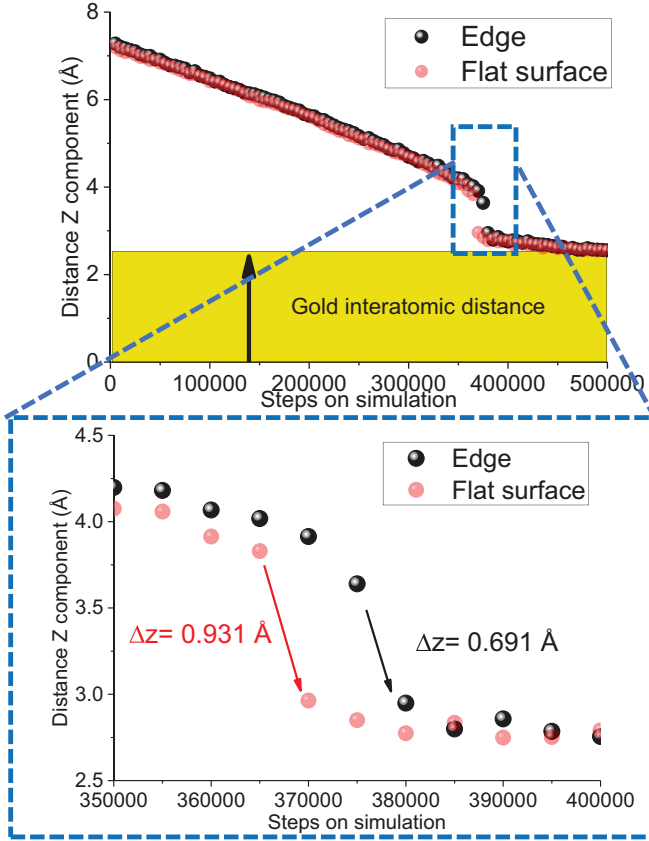
FIG. 4. Vertical distance between tip apex atom and adatom vs simulation time step. Black dots correspond to the adatom on a edge scenario, and red dots correspond to adatoms close to the flat surface. Inset: A zoom-in of the distance traces near the moment when contact first occurs.

the adatom is on the flat surface, the jump distance is larger and more abrupt.

Upon analyzing all the calculated distance traces, we obtain the vertical atomic distance in contact (contact distance), the distance prior to contact (tunnel distance), and the difference between these two distances Δz. Tables III and IV show these CMD results in the first four columns, for the

TABLE III. Molecular dynamics and conductance calculations via DFT+NEGF for the **Edge** scenario.

Cycle	z tun. (Å)	z con. (Å)	Δz (Å)	G_t (G_0)	G_c (G_0)
01	3.74	2.87	0.87	0.30	0.94
02	3.64	2.93	0.70	0.32	0.83
03	3.65	2.94	0.71	0.38	0.86
04	3.66	2.92	0.75	0.34	0.86
05	3.64	2.95	0.69	0.36	0.85
06	3.62	2.93	0.69	0.35	0.87
07	3.53	2.92	0.61	0.39	0.84
08	3.77	3.31	0.47	0.27	0.58
09	3.60	2.95	0.65	0.36	0.82
10	3.53	2.90	0.62	0.45	0.83

TABLE IV. Molecular dynamics and conductance calculations via DFT+NEGF for **Flat surface** scenario.

Cycle	z tun. (Å)	z con. (Å)	Δz (Å)	G_t (G_0)	G_c (G_0)
01	3.71	2.97	0.74	0.23	0.84
02	3.77	2.98	0.79	0.28	0.81
03	3.89	2.88	1.01	0.23	0.92
04	3.78	2.89	0.89	0.32	0.87
05	3.89	2.96	0.93	0.27	0.87
06	3.82	2.76	1.06	0.24	0.93
07	3.76	2.80	0.96	0.34	0.95
08	3.76	2.84	0.92	0.34	0.94
09	3.80	2.89	0.91	0.30	0.89
10	3.76	3.05	0.71	0.33	0.84

edge and flat surface scenarios, respectively. The first column corresponds to the contact cycle, the second and third columns show respectively the distance (in Å) between the adatom and the apex atom of the tip in the tunneling and contact regimes. The fourth column shows the jump distance Δz in going from tunneling to contact. Finally, the last two columns contain the results of conductance calculations in units of G_0 obtained via DFT+NEGF transport for tunneling and contact regime, respectively.

From Table III, the mean distance between the apex atom and the adatom at the jump to contact, averaged over the ten cycles, is 3.64 ± 0.08 Å, while after contact has been established, it is 2.96 ± 0.12 Å, with the mean jump distance 0.68 ± 0.1 Å. For the 10 cycles for the flat surface, the mean distance before the jump is 3.79 ± 0.06 Å, after contact it is 2.89 ± 0.08 Å, and the mean jump distance is 0.89 ± 0.11 Å. We summarize in Table V these averaged results from Tables III and IV. The first column indicates the scenario, edge, or flat surface. The second column shows the mean value and standard deviation of Δz, and the third and fourth columns show the mean value and standard deviation of G_t and G_c, respectively.

VI. DISCUSSION

In this section we will discuss how the atomic level detail of the mechanical properties of the environment at the junction can effect the dynamic bonding behavior.

A. Effect of variations in the surface structure

To assess how the change in the surface affects the dynamic bonding, we have studied two scenarios as mentioned earlier. In both the scenarios a STM tip is made to approach from

TABLE V. Mean values and standard deviations of Δz, G_t and G_c of the data shown in Tables III and IV.

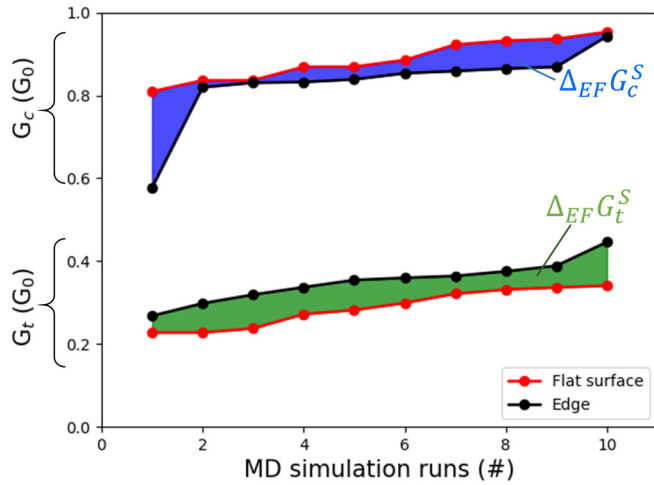| Scenario	Δz (Å)	G_t (G_0)	G_c (G_0)
Edge	0.68 ± 0.10	0.35 ± 0.05	0.83 ± 0.09
Flat surface	0.89 ± 0.11	0.29 ± 0.04	0.89 ± 0.05

FIG. 5. Line plots showing sorted G_t and G_c values of calculated conductance for flat surface (red) and step edge (black). Blue shows the difference (Δ) between calculated conductance of the contact (G_c^S) for the flat surface and edge (F and E sub-index). Green region correspond on the difference difference (Δ) between calculated conductance of the tunneling regime (G_t^S) for the flat surface and edge.

above an adatom placed on top of (1) a flat Au (111) surface and (2) a monoatomic step edge created over a Au(111) surface. All the corresponding simulation cycles (as discussed in the previous section) were performed using the same ideal crystalline pyramidal tip structure. This helps in avoiding any effect of variations in tip structures at this moment, and, as a result, the variation in the simulation results comes entirely from the small temperature fluctuations. Therefore, because the temperature fluctuations are completely random in our ergodic simulations within the canonical-ensemble [39,45,46], we can, for convenience, sort the G_t and G_c values given in Tables III and IV in ascending order. We can then plot a combined line plot with conductance on the vertical axis and count index (ranging from 1 to 9) on the horizontal axis for both the scenarios (black for edge and red for flat surface); see Fig. 5.

Comparing the results for the flat surface and edge case of Fig. 5, we observe that the mean value of G_t is higher in the case of the edge. The mean G_c values are however very similar in both the scenarios, with marginally higher numbers for the flat surface. The marginally higher G_c values for the flat surface can be understood by higher coordination value [25] of the point contact in case of the flat surface. A similar state of affairs is expected for the G_t values, which should exhibit a slightly lower value in the case of the simulated step edge. However, what we observe in our simulations is rather the opposite. We show a similar conclusion derived also from experiments in the next section. Up to this point, we cannot discern whether it is a consequence of the geometrical configuration or attributable to a difference in the density of states.

To understand the origin of the high values of G_t in the edge scenario, we consider two main hypotheses. The first is based on the Smoluchowski effect [54], an electronic effect in which the adatom is a tightly bound surface dipole, leading to

the adatom being held more strongly on the flat surface than at the edge, with lower tunneling conductance as a result.

The second hypothesis is based on a geometric effect and mechanical surface properties, in which the tip pulls on the adatom as it approaches it, with the adatom in turn pulling on the atoms of the step edge, bending the surface toward the tip. To explore both hypotheses, we have selected the following atomic geometry configurations, cycles 3 and 5 for edge case and flat surface, respectively. We have selected these cycles since the G_c values are quite similar but the G_t is almost twice as high in the case of the edge than the flat surface.

To explore the role of the Smoluchowski effect, we have performed total energy calculations in QUANTUM ESPRESSO [55] on the edge and flat surface structures from our CMD simulations, excluding the tips. Based on the difficulty of calculating reliable surface states using (unreconstructed) surfaces obtained from CMD and dealing properly with periodic boundary conditions for large supercells in DFT calculations, we have used supercells of unreconstructed (111) surfaces, trimmed down to ~200 atoms from our CMD structures, with a rhombus base for correct boundary conditions.

Therefore, as in most of our quantum transport calculations, we did not further relax the atoms and here simply used the respective atomic structure snapshots from the CMD simulations at the point directly prior to jumping into contact, and directly after, and calculated the total energy of the CMD snapshots. We used the Perdew-Zunger LDA exchange-correlation functional [56] and an ultrasoft pseudopotential that has been benchmarked against all-electron calculations [57]. We also verified the convergence of the total energy as a function of k-point sampling in the irreducible wedge of the Brillouin zone. A $2 \times 2 \times 2$ Monkhorst-Pack mesh provided good convergence given the size of the rhombohedral supercell ($\approx 27.0 \times 22.0 \times 24.0$ Å^3).

In Fig. 6, we thus show electronic density difference contours on planes through the center of the adatom along the long diagonal of the rhombus-based supercell on the adatom-surface systems. Figure 6(a) corresponds to the case of a flat surface, and Fig. 6(b) corresponds to the adatom near an edge. Moreover, Fig. 6 shows in both cases that the adatom shares significantly more electron density with its neighbours in the threefold (111) hollow (see the blue contour lines), than for the other atoms on the surface. Only one of these three neighbors appears in each of the plots. In Fig. 6(b), the neighbor located at the edge is included in the cross-section. The role of the Smoluchowski effect [54] therefore is similar in both cases, i.e., strong surface dipoles form on both surfaces about the adatom, and hence cannot explain the observed differences between mean G_t values in edge and flat surface.

After discarding the Smoluchowski effect, we explore the second hypothesis. We analyze the deformations over the surface that occurs when the adatom is attracted by the apex atoms for the simulated cycles 3 and 5. In this analysis, we plot the trajectory along the z axis of the adatom and its first neighbors to the right, left, front and an atom that is distant from the point contact. Figure 7 shows the trajectories of these atoms using different colors.

As reference, we have selected the distant atom from the same row of atoms, which has been color-coded black. The upper panel in Fig. 7 shows the trajectories for the edge
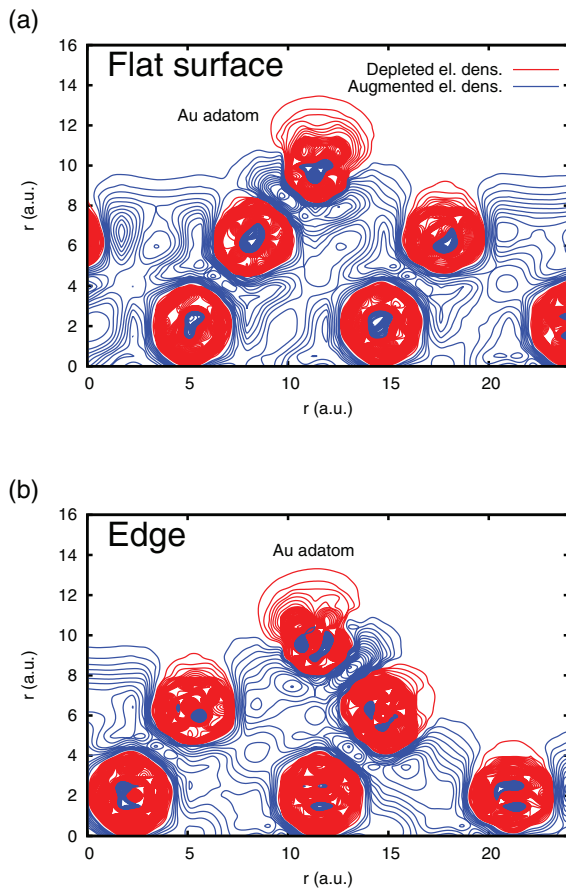
(a)

(b)

FIG. 6. Electronic density difference contours on planes passing through the center of an adatom on (a) a gold flat surface and (b) near a step edge along the long diagonal of the rhombus-based (111) supercell used in the total energy DFT calculation. Red and blue contours correspond to equally spaced negative and positive values of the electron density difference, representing regions depleted of and augmented with electron density relative to free Au atoms, respectively.

scenario and the bottom panel corresponds to the flat-surface case. The insets to the right of each panel of trajectories depict the two scenarios. Dashed lines guide the eye to identify the atoms corresponding to the trajectories. Furthermore, the yellow arrows indicate the relative movement of the two surfaces and tips. According to the movement of the surface all the trajectories are ascending slopes. For all the first neighbors as well as the adatom trajectories, we observe a jump in the trend of the slope. This jump occurs when the adatom jumps to make contact with the apex atom of the tip. That the neighbor atoms also undergo a jump confirms that the surfaces are deformed by the forces that pull on the adatom. However, we observe that in both cases the distant atom does not suffer such a jump and, as a consequence, its adjoining borders are not deformed.

Compared to the bottom panel, the trajectories of the first neighbor atoms in the upper panel clearly deviate more from that of the distant atom used as reference. This is not surprising since the edge is expected to deform more easily than the flat surface under the attractive force of the descending tip. Nevertheless, to understand the mechanical effects in greater
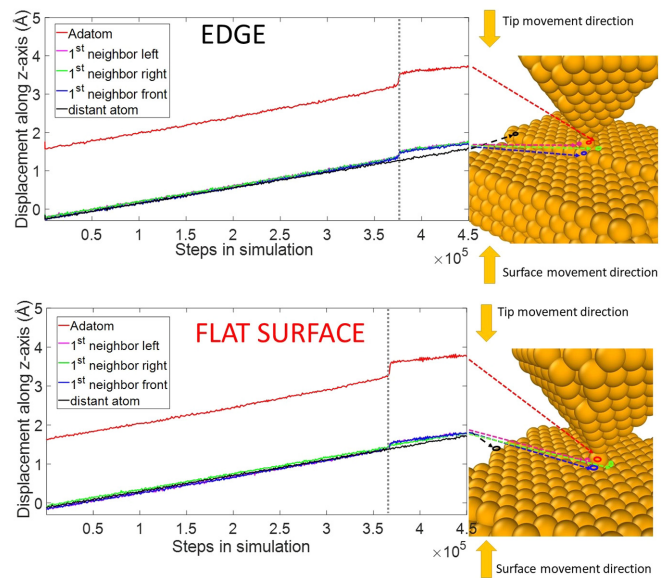

FIG. 7. Top and bottom panels correspond to the trajectories along the z-axis of selected atoms in the depictions of the edge and flat surface shown on the right in the insets. Red, pink, green, blue, and black lines are the trajectories of the adatom as well as its first neighbors to the right, left, front, and a distant atom.

detail, we have analyzed the deformation difference of the trajectory, which we have obtained by subtracting the slope of every trajectory from the trajectories themselves, as Fig. 8 shows. Therefore, Fig. 8 illustrates the deformation of the adatom and neighboring atoms relative to the "bulk" of the substrate. Within this analysis, the upper and lower panels show the deformation of the edge and flat surface, respectively. The colored lines refer to the same atoms as in Fig. 7.
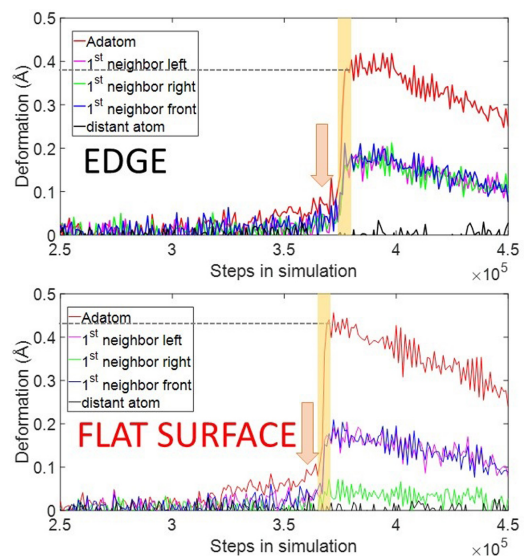

FIG. 8. Top and bottom panels correspond to the deformation of the trajectory calculated from the subtraction of the slope of the trajectory from the trajectory itself. Upper panel corresponds to edge and bottom to flat surface scenario. The colors of the traces refer to the same atoms as in the previous figure.

The vertical yellow highlighted areas brings attention to the abrupt deformation that occurs in all the curves. Figure 8 further underlines the conclusions we drew about the distance traces in Fig. 7 in that not only the adatom, but also its neighbors, are deformed by the forces pulling on the adatom. As expected, the distant atom (black traces in Fig. 8) does not exhibit a deformation over the trend in its trajectory. Considering the deformation of the three first neighbors of the adatom, to the front (blue), left (pink), and right (green), we see that in the case of an adatom at the edge, all first neighbors undergo a similar deformation during the jump to contact. In contrast, for the adatom in the the flat surface region, while the front and left adatoms undergo similar deformations as in the edge case, the right neighbor in the flat case (green) undergoes a much smaller deformation (∼4 times smaller) than in the edge case. The asymmetric deformation of the three first neighbors in this case is due to the vertical alignment of the tip apex atom and adatom not being perfect as a result of thermal fluctuations in the CMD simulations. This also implies that the right neighbor will not contribute to the tunneling current to the same extent in the flat surface case as in the edge case [25]. Therefore, while all three neighbors fully contribute to the tunneling current for the edge case, only two neighbors will substantially contribute to the tunneling current in the flat surface case. This explains why the mean value of G_t is lower for the flat surface than the edge in Table V. Note also that all the calculated tunneling conductance values are an order of magnitude larger than in the experiments because the CMD simulations cannot fully account for the particularly strong force between gold atoms arising due to scalar relativistic effects [24].

An additional striking feature of Fig. 8 is marked by the arrow, which indicates where the deformation preceding the jump-to-contact commences. In the case of the edge all the deformation curves of the first neighbors follow the deformation trend of the adatom, increasing smoothly before the abrupt jump occurs. However, in the case of the flat-surface the adatom starts to deform significantly earlier than the neighboring atoms, which only start to deform once the abrupt jump-to-contact occurs. An immediate conclusion is that on the flat surface the adatom initiates a deformation earlier and its first neighbors are not affected in the early stages of this process; they are only affected a few steps before the jump to contact of the adatom occurs. This transition is a consequence of the fact that the flat surface deforms less readily than the edge. Recall that we found the strength of the Smoluchowski effect to be similar in both situations, and that the adatom is therefore bound nearly equally strongly on both surface types. So, early in the contact making phase, unlike on the edge, the adatom on the flat surface is not accompanied by its nearest neighbours during the deformation process. It is clear that the greater relative freedom of the adatom in the flat surface case allows this adatom to perform a larger vertical excursion (Δz) and approach the tip apex more closely than in the edge case.

B. Effect of variations in experimental STM tip structure

In the theoretical models discussed in the previous section, we have assumed a well-defined pyramidal STM tip and have shown how small changes in the mechanical deformations on
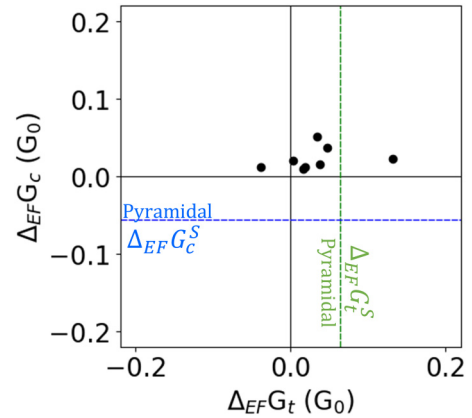

FIG. 9. Experimental data of $\Delta_{\mathrm{EF}}G_c$ vs. $\Delta_{\mathrm{EF}}G_t$. Green and blue dashed lines mark the position of $\Delta_{\mathrm{EF}}G_t^S$ and $\Delta_{\mathrm{EF}}G_c^S$ values extracted for an ideal pyramidal tip from *ab inito* calculations.

the surface have significant impact on the dynamic bonding and associated conduction measurements. However, experimentally, the structure of the STM tips is usually unknown and is always a matter of concern in any atomic scale electronic transport measurements [58]. There are techniques to train the shape of the tip apex up to one or two atomic layers [10,35], and it is usually assumed that as the tunneling current drops exponentially with distance, the tip structure behind the apex should not play a significant role.

To facilitate a comparison with the experiment of the *ab initio* data shown in Fig. 5 in the two scenarios, we have studied the difference between experimental and calculated mean values of G_t and G_c.

In Table I, we collect the conductance data of first contact and last value of tunneling, extracted from 8 experimental traces of conductance, where each set consists of measurement on top of the flat surface and then on top of the step edge. During each set of experiments comprising a measurement at the edge and a measurement at the flat surface, we avoided changes in the tip apex structure [35]. Then the tip was retrained by means of the mechanical annealing technique [10,35] before the next set of experiments were conducted. To compare the experimental results with our calculations, we have defined a parameter Δ_{EF}, which is the difference between the experimental conductance values of edge and the flat surface scenarios within each set, i.e., $\Delta_{\mathrm{EF}} = G_{\mathrm{Edge}} - G_{\mathrm{Flat\ Surface}}$. Δ_{EF} values are calculated separately for the tunneling ($\Delta_{\mathrm{EF}}G_t$) and first contact conductance values ($\Delta_{\mathrm{EF}}G_c$). These are then plotted in a $\Delta_{\mathrm{EF}}G_c$ versus $\Delta_{\mathrm{EF}}G_t$ plot in Fig. 9. The black dots represent the experimental data points. We have also plotted blue and green dashed lines which represent the mean Δ_{EF} values obtained from the simulation data shown in Fig. 5. These are called $\Delta_{\mathrm{EF}}G_c^S$ and $\Delta_{\mathrm{EF}}G_t^S$, where the superscript "S" signifies that these are obtained from the simulated data using a pyramidal tip.

Considering that the tip apex structure in all the experiments can be assumed similar to a one or two layer pyramidal structure, we would expect that the $\Delta_{\mathrm{EF}}G_t$ and $\Delta_{\mathrm{EF}}G_c$ values would be comparable to those from the theoretical simulations. Indeed, we do see some similarities, like the $\Delta_{\mathrm{EF}}G_t$ values obtained experimentally are mostly positive similar to

the simulation (green dashed line) and which could be explained by the extra bulging of the surface at the step edge also discussed earlier. However, the experimental values still differ significantly from the simulation. In this regard, we highlight that our calculated G_c values are underestimated by $\sim$5–10% because our DFT quantum transport method does not account for surface states [59], the implementation of which we leave for future work. Nevertheless, surface states are expected to be present in both cases, though should contribute less to the calculated conductance in the edge scenario. So, in calculating $\Delta_{EF} G_c^S$, surface state effects should cancel out to some degree. After accounting for the limitations of our calculations, our combined theoretical and experimental results suggest that although in our controlled experiments the tip apex structure was trained, the experimental tip would be very different from the ideal pyramidal structure far from the tip apex. This would confer different mechanical properties to the experimental tips and they would thus behave differently in the dynamic bonding experiments.

Such an analysis therefore also helps to establish whether an experimental tip would be closer to an ideal crystalline pyramidal tip. So, with such controlled tests we can get an idea that the plausible structure of the experimental tips for which the $\Delta_{EF} G_t$ and $\Delta_{EF} G_c$ values would fall close to the simulated values ($\Delta_{EF} G_c^S$ and $\Delta_{EF} G_t^S$), should be then closer to the ideal pyramidal tip structure even far from the tip apex or at least shares similar mechanical properties.

VII. CONCLUSIONS

In this work, we have shown that repeated approach cycles of atomic-sized tips on adatoms either close to a monatomic step edge, or in an atomically flat surface region far from any step edge on Au (111) facets, exhibit dispersion in both theoretical and experimental conductance data. This fact reveals that small changes in the surroundings of the adatom and tip affect the conductance during the pre- and first-contact processes.

In the first experimental scenario, an adatom was placed on a flat Au(111) surface and approached from above by an STM tip. In the second scenario, the adatom was placed at a monoatomic step edge and the same procedure with the STM tip was repeated. Both the experiments and theoretical simulations showed that tunneling conductance (G_t) just before the jump-to-contact was larger in the presence of the step edge, which could be considered counter intuitive. We explained this difference in G_t values under the two scenarios by appealing to a hypothesis involving the role of the geometry of the two surfaces.

Furthermore, we showed that as the "dynamic bonding" behavior is sensitive to fine adjustments in the mechanical properties of the junction, we can use it to extract insights about the STM tip beyond just the apex of the tip. Finally, the demonstrated sensitivity of the dynamical bonding of the STM tip (and the associated conductances) as a function of deformation and local environment at the atomic level, can contribute to the advancement and improve understanding of the interaction of STM tips with atomic-scale structures in the emerging field of straintronics.

[1] G. Binnig, H. Rohrer, C. Gerber, and E. Weibel, Phys. Rev. Lett. **49**, 57 (1982).

[2] G. Binnig and H. Rohrer, Rev. Mod. Phys. **59**, 615 (1987).

[3] M. Herz, F. J. Giessibl, and J. Mannhart, Phys. Rev. B **68**, 045301 (2003).

[4] I. Battisti, G. Verdoes, K. van Oosten, K. M. Bastiaans, and M. P. Allan, Rev. Sci. Instrum. **89**, 123705 (2018).

[5] D. M. Eigler and E. K. Schweizer, Nature (London) **344**, 524 (1990).

[6] J. A. Stroscio and D. M. Eigler, Science **254**, 1319 (1991).

[7] M. F. Crommie, C. P. Lutz, and D. M. Eigler, Science **262**, 218 (1993).

[8] S. W. Hla, Rep. Prog. Phys. **77**, 056502 (2014).

[9] F. E. Kalff, M. P. Rebergen, E. Fahrenfort, J. Girovsky, R. Toskovic, J. L. Lado, J. Fernández-Rossier, and A. F. Otte, Nat. Nanotechnol. **11**, 926 (2016).

[10] C. Sabater, C. Untiedt, J. J. Palacios, and M. J. Caturla, Phys. Rev. Lett. **108**, 205502 (2012).

[11] R. Landauer, IBM J. Res. Dev. **1**, 223 (1957).

[12] L. Limot, J. Kröger, R. Berndt, A. Garcia-Lekue, and W. A. Hofer, Phys. Rev. Lett. **94**, 126102 (2005).

[13] J. Kröger, N. Néel, and L. Limot, J. Phys.: Condens. Matter **20**, 223001 (2008).

[14] C. Muller, J. van Ruitenbeek, and L. de Jongh, Physica C **191**, 485 (1992).

[15] J. M. Krans, C. J. Muller, I. K. Yanson, T. C. M. Govaert, R. Hesper, and J. M. van Ruitenbeek, Phys. Rev. B **48**, 14721 (1993).

[16] B. Pabi, D. Mondal, P. Mahadevan, and A. N. Pal, Phys. Rev. B **104**, L121407 (2021).

[17] N. Agraït, J. G. Rodrigo, and S. Vieira, Phys. Rev. B **47**, 12345 (1993).

[18] J. I. Pascual, J. Méndez, J. Gómez-Herrero, A. M. Baró, N. García, and V. T. Binh, Phys. Rev. Lett. **71**, 1852 (1993).

[19] N. Agraït, A. L. Yeyati, and J. M. Van Ruitenbeek, Phys. Rep. **377**, 81 (2003).

[20] M. L. Trouwborst, E. H. Huisman, F. L. Bakker, S. J. van der Molen, and B. J. van Wees, Phys. Rev. Lett. **100**, 175502 (2008).

[21] M. Müller, C. Salgado, N. Néel, J. J. Palacios, and J. Kröger, Phys. Rev. B **93**, 235402 (2016).

[22] C. Untiedt, M. J. Caturla, M. R. Calvo, J. J. Palacios, R. C. Segers, and J. M. van Ruitenbeek, Phys. Rev. Lett. **98**, 206801 (2007).

[23] C. Sabater, M. J. Caturla, J. J. Palacios, and C. Untiedt, Nanoscale Res. Lett. **8**, 257 (2013).

[24] M. R. Calvo, C. Sabater, W. Dednam, E. B. Lombardi, M. J. Caturla, and C. Untiedt, Phys. Rev. Lett. **120**, 076802 (2018).

[25] C. Sabater, W. Dednam, M. R. Calvo, M. A. Fernández, C. Untiedt, and M. J. Caturla, Phys. Rev. B **97**, 075418 (2018).

[26] M. A. Fernández, C. Sabater, W. Dednam, J. J. Palacios, M. R. Calvo, C. Untiedt, and M. J. Caturla, Phys. Rev. B **93**, 085437 (2016).

[27] D. van Vreumingen, S. Tewari, F. Verbeek, and J. M. van Ruitenbeek, Micromachines **9**, 270 (2018).

[28] S. Tewari, Molecular electronics: controlled manipulation, noise and graphene architecture, Ph.D. thesis, Leiden Institute of Physics (LION), Leiden University (2018).

[29] S. Tewari, J. Bakermans, C. Wagner, F. Galli, and J. M. van Ruitenbeek, Beilstein J. Nanotechnol. **10**, 337 (2019).

[30] D. J. Oliver, W. Paul, M. E. Ouali, T. Hagedorn, Y. Miyahara, Y. Qi, and P. H. Grütter, Nanotechnology **25**, 025701 (2014).

[31] F. Moresco, L. Gross, M. Alemani, K.-H. Rieder, H. Tang, A. Gourdon, and C. Joachim, Phys. Rev. Lett. **91**, 036601 (2003).

[32] F. Moresco, Phys. Rep. **399**, 175 (2004).

[33] F. Moresco, L. Gross, L. Grill, M. Alemani, A. Gourdon, C. Joachim, and K. Rieder, Appl. Phys. A **80**, 913 (2005).

[34] A. Castellanos-Gomez, G. Rubio-Bollinger, M. Garnica, S. Barja, A. L. Vázquez de Parga, R. Miranda, and N. Agraït, Ultramicroscopy **122**, 1 (2012).

[35] S. Tewari, K. Bastiaans, M. Allan, and J. van Ruitenbeek, Beilstein J. Nanotechnol. **8**, 2389 (2017).

[36] J. Yang, D. Sordes, M. Kolmer, D. Martrou, and C. Joachim, Eur. Phys. J. Appl. Phys. **73**, 10702 (2016).

[37] J. Wintterlin, J. Wiechers, H. Brune, T. Gritsch, H. Höfer, and R. J. Behm, Phys. Rev. Lett. **62**, 59 (1989).

[38] M. P. Allen and D. J. Tildesley, *Computer Simulation of Liquids* (Oxford University Press, Oxford, UK, 1989).

[39] D. Frenkel and B. Smit, *Understanding Molecular Simulation: From Algorithms to Applications* (Academic Press, San Diego, CA, 2002).

[40] M. S. Daw and M. I. Baskes, Phys. Rev. Lett. **50**, 1285 (1983).

[41] X. Zhou, H. Wadley, R. A. Johnson, D. Larson, N. Tabat, A. Cerezo, A. Petford-Long, G. Smith, P. Clifton, R. Martens *et al.*, Acta Mater. **49**, 4005 (2001).

[42] H. Wadley, X. Zhou, R. Johnson, and M. Neurock, Prog. Mater. Sci. **46**, 329 (2001).

[43] S. Plimpton, J. Comput. Phys. **117**, 1 (1995).

[44] S. Plimpton *et al.*, Computer code LAMMPS, publicly available at http://lammps.sandia.gov.

[45] S. Nosé, Mol. Phys. **52**, 255 (1984).

[46] W. G. Hoover, Phys. Rev. A **31**, 1695 (1985).

[47] W. C. Swope, J. Chem. Phys. **76**, 637 (1982).

[48] J. J. Palacios, A. J. Pérez-Jiménez, E. Louis, and J. A. Vergés, Phys. Rev. B **64**, 115411 (2001).

[49] J. J. Palacios, A. J. Pérez-Jiménez, E. Louis, E. San Fabián, and J. A. Vergés, Phys. Rev. B **66**, 035322 (2002).

[50] E. Louis, J. A. Vergés, J. J. Palacios, A. J. Pérez-Jiménez, and E. San Fabián, Phys. Rev. B **67**, 155321 (2003).

[51] J. J. Palacios *et al.*, Computer code ANT.Gaussian, publicly available at https://www.simuneatomistics.com/products/ant/ and https://github.com/juanjosepalacios/ANT.Gaussian.

[52] M. J. Frisch *et al.*, Computer code GAUSSIAN09, Revision C.01 (Gaussian, Inc., Wallingford, CT, 2009).

[53] W. Dednam, C. Sabater, M. A. Fernandez, C. Untiedt, J. J. Palacios, and M. J. Caturla, J. Phys.: Conf. Ser. **574**, 012045 (2015).

[54] H. Ibach, *Physics of Surfaces and Interfaces*, Vol. 12 (Springer, Berlin, 2006).

[55] P. Giannozzi *et al.*, J. Phys.: Condens. Matter **21**, 395502 (2009).

[56] J. P. Perdew and A. Zunger, Phys. Rev. B **23**, 5048 (1981).

[57] K. Lejaeghere *et al.*, Science **351**, aad3000 (2016).

[58] F. Evers, R. Korytár, S. Tewari, and J. M. van Ruitenbeek, Rev. Mod. Phys. **92**, 035001 (2020).

[59] D. Li, J. L. Bertelsen, N. Papior, A. Smogunov, and M. Brandbyge, Phys. Rev. Res. **3**, 033017 (2021).